This is a postprint version of the following published document:

Proyectos:

Numerical analysis of CFRP fluid-filled tubes subjected to high-velocity impact

J.A. Artero-Guerrero, J. Pernas-Sánchez, D. Varas,

J. López-Puente *

Department of Continuum Mechanics and Structural Analysis. University Carlos III of Madrid. Avda. de la Universidad, 30. 28911 Leganés, Madrid, Spain

Abstract

In recent years, vulnerability against high-velocity impact loads has become an increasingly critical issue in the design of composite aerospace structures. The effects of Hydrodynamic Ram (HRAM), a phenomenon that occurs when a high-energy object penetrates a fluid-filled container, are of particular concern in the design of wing fuel tanks for aircraft because it has been identified as one of the important factors in aircraft vulnerability. The projectile transfers its momentum and kinetic energy through the fluid to the surrounding structure, increasing the risk of catastrophic failure. In the present paper, the commercial finite-element code

* Corresponding author. Fax number: 34 916248331. E-mail address: jlpuente@ing.uc3m.es

ABAQUS/Explicit has been used to simulate an HRAM event due to the impact of a steel spherical projectile into a water-filled woven CFRP square tube. In order to simulate the fluid-structure interaction, the Coupled Eulerian Lagrangian (CEL) approach is used. Experimental tests which indicate the pressure at different points of the fluid, strains of the walls and cavity evolution for different impact velocities are compared with the numerical results in order to assess the validity and accuracy of CEL technique in reproducing such a complex phenomenon. Also, several numerical impacts at different initial projectile velocities are performed to study its influence in the HRAM phenomenon.

1   Introduction

Nowadays the aeronautical and aerospace industries are continuously increasing the usage of laminated composite structures to diminish the fuel consumption. The choice of this kind of materials is due to the high strength-to-weight and stiffness-to-weight ratios as well as their anisotropic behavior. Those special characteristics allow to optimize designs and fulfil the strict requirements of the mentioned industries with a reduction of the total mass of the structure and hence saving fuel. The most used composite materials for structural applications in these sectors are carbon fiber reinforced plastics (CFRP), commonly manufactured with an epoxy matrix that combines good mechanical properties, high resistance to corrosion and fatigue, and low density (ρ=1500 kg/m^3). The reduction of raw material costs, the development of automation of manufacturing processes, and the growing experience in design technology have increased the CFRP applications in commercial aircraft [1], such as the fuselage and wings, so that in the last designs of aeronautical structures this kind of materials constitutes more than the 50% (in terms of weight). The successful usage of these materials in primary structures depends on understanding their response to a wide range of impact loadings. The study of the

behavior of composite laminates under high-velocity impact has received attention since the 1970s, when only military research agencies where concerned about this subject. In the 1980s, investigators from civil organizations began to publish articles in which the breakage mechanism of such materials under ballistic impact was investigated primarily from an experimental approach [2–4]. Later, both analytical [5–11] and numerical [12–17] approaches were used to predict the energy absorbed by the laminate in a penetrating impact and the damaged area.

Vulnerability studies of CFRP aerospace structures are becoming an issue of great importance in the design of any aircraft [8]. These structures may suffer high velocity impact loads due to bird strikes [18] or hailstones [19], especially dangerous because of their high possibility of occurrence and their disastrous consequences. Runway debris may impact the underside of the wing structures [20] causing hydrodynamic ram effects in the fuel tanks, which are considered one of the most important factors in aircraft vulnerability.

The hydrodynamic ram (HRAM) phenomenon appears when an object with high kinetic energy penetrates a fluid-filled tank and transfers its kinetic energy through the fluid to the surrounding structure, increasing the risk of catastrophic failure and excessive structural damage. HRAM is particularly dangerous for aircrafts with lightweight designs, because the structural resistance of their integral fuel tanks cannot be improved by strengthening the airframe; strengthening the frame would counteract the requirements of a lightweight design. Vulnerability to HRAM has been usually related to military aircraft, but commercial airplanes are not exempt of its effect. In 1990 the Federal Aviation Administration (FAA) established the Aircraft Catastrophic Failure Prevention Research Program in which the analysis of the effects of an uncontained turbine engine fragment penetrating commercial aircraft fuel tanks [21] was carried on. An example of the importance of the HRAM phenomenon is the Concorde accident that occurred in 2000. The final investigation

report revealed that the HRAM had played a significant role in the aircraft failure.

The study of the HRAM phenomenon is not only important for the aircraft industry. High velocity impacts on fluid filled containers are of great interest for different industrial fields such as safety of industrial facilities or road haulage, where containers are commonly used to store fuel or dangerous products. In those cases, an impact in the vessel may produce the failure of the tank and could result in a serious consequences on the environment or even toxic and flammability effects [22–24].

Hydrodynamic Ram consists of four principal stages: shock, drag, cavitation and exit. Each stage contributes to structural damage through a different mechanism and to a different extent. When the projectile penetrates the wall of the fluid filled structure, the impact energy is transferred to the fluid and generates a high-pressure hemispherical shock wave. This leads to damage primarily in the vicinity of the impact position. During the drag phase, the projectile travels through the fluid, and its kinetic energy is partially transformed into fluid motion as the projectile is slowed by viscous drag. The displacement of the fluid from the projectile path generates a radial pressure field. In contrast to the pressure field developed during the shock phase, the fluid is accelerated gradually rather than impulsively. This causes less intense peak pressures, but they are of greater temporal extent. The displacement of fluid during the drag stage forms a cavity behind the projectile. The subsequent expansion and collapse (oscillations) of the cavity is known as the cavitation stage. The oscillations of the cavity can cause significant pressure pulses. The final stage of Hydrodynamic Ram occurs when the projectile exits the container. In contrast to the perforation of the front wall, the exit of the projectile occurs through a pre-stressed wall. The pre-stress is caused by the initial shock stage and the subsequent loading by the fluid.

Simulation of HRAM events has been attempted, with more or less success, for over 30 years. The first methods were based on the use of the *Piston Theory* [25,26]

and the *Variable Image Method* [27] for the fluid-structure interaction. Once these methods were proven to not provide a realistic coupling between the fluid and the structure, other codes such as HRSR (Hydraulic Ram Structural Response) [28], ERAM or EHRSR were developed [29], but all of them showed limitations on simulating an HRAM event since none of them fully coupled the mechanisms of fluid-structure interaction and were limited to simple structures. The complicated physics and mechanics of HRAM phenomena were not satisfactory solved until higher-order numerical algorithms were incorporated into the codes in the late 1980´s. Coupled Euler-Lagrange (CEL) methods have been under development since the early-to-mid 1990´s. They combine the desirable characteristics of Lagrangian and Eulerian formulations so that the distortion problems in the fluid are avoided due to the Eulerian approach as well as the limits of the structure are perfectly reproduced by means of the Lagrangian formulation. These methods are used in multiple industries for a wide variety of analysis in which fluids interact with structures or when high distortions may appear [21,30–37], including airbag and tire-water dynamics in the automobile field [38,39], the impact of bird strikes on aircraft [40,41], and the effects of sloshing on ships [42].

In the last years and motivated by different industries such as aeronautics, naval or more recently biomedical sciences, there have been new advances in development and use of computational methods for fluid-structure interactions in order to reach more effective computational techniques [43–48] and solving more difficult problems. As an example of the increasing interest on solving industrial fluid-structure problems the works of Petitpas et al. [49] or Lecysyn et al. [22,23] can be mentioned, in which a ballistic impact on an industrial tank, filled with a toxic fluid, is studied.

The simulation of coupled problems of fluid-structure interaction such as HRAM added to the modelling of carbon fiber composites, has been proven to be a complicated task and is still quite challenging [51,50]. The suitability and predictive

capabilities of different techniques (CEL, ALE or SPH) in an HRAM problem have not yet been solved. This is of great importance since analytical solutions can provide only a limited understanding of the nature of the behaviour.

In the present work, numerical simulations of a water-filled CFRP square tube subjected to impact by steel spherical projectiles at different velocities are shown. The simulations are performed with the commercial code ABAQUS/Explicit V.6.10 using a coupled eulerian-lagrangian (CEL) approach to reproduce the fluid-structure interaction produced as a consequence of the HRAM phenomenon. In addition a woven CFRP material model is implemented by means of an user subroutine to appropriately reproduce the behavior of the structure. Experimental tests data regarding pressure in different points of the fluid, cavity evolution for different impact velocities and the failure of the walls are compared with the numerical results in order to assess the validity and accuracy of the proposed numerical model in reproducing such a complex phenomenon.
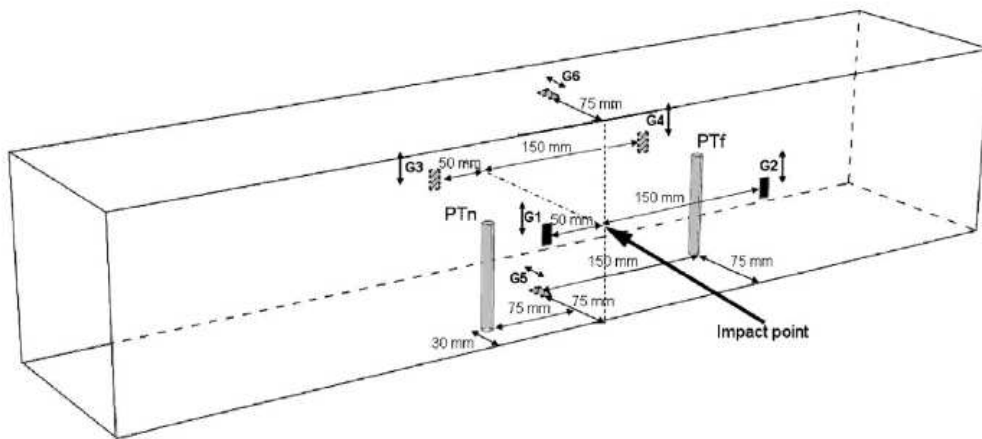
2 Experimental setup

In order to achieve an appropriate and wide validation of the numerical model, the same authors of this work performed experimental tests to obtain data on pressure, cavity evolution and failure of the CFRP structure due to the HRAM phenomenon. The experimental results were presented in a previous paper [52]. These tests consisted on high velocity steel sphere impacts against a woven CFRP tube filled with water. In Fig. 1 (a) the sketch of the experimental device used in the mentioned tests can be seen.

The specimen into which projectiles were impacted corresponds to square woven CFRP tubes 150 mm wide, 2.2 mm thick and 750 mm long. The composite woven laminated selected was the AGP-193-PW manufactured by Hexcel Composite, com-
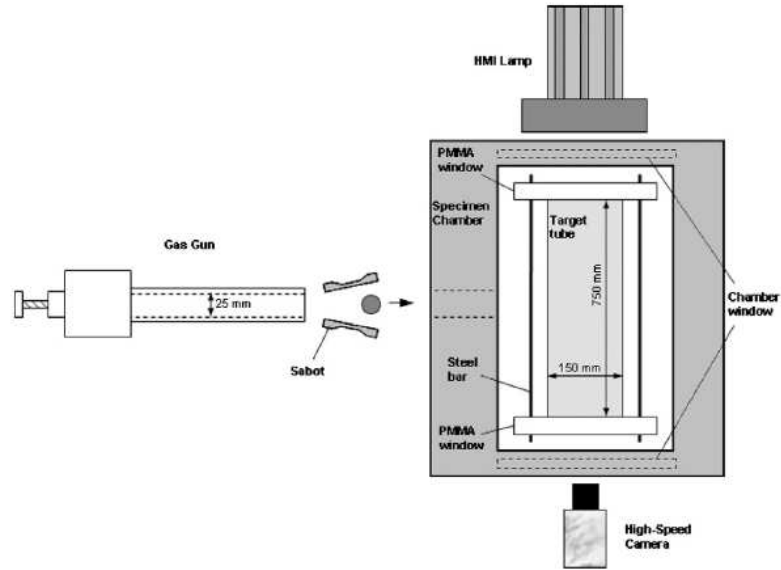
(a)

(b)

Fig. 1. (a) Sketch of the experimental setup (b) Sketch of the CFRP tube instrumented

posed by 10 plies ($[0]_{10}$). Each ply is made with a plain weave of $AS4$ fibers and the 8552 resin. The tube was closed with two PMMA windows, 30 mm thick, fixed with four steel bars; through these windows, the whole impact and penetration process was recorded by means of a Photron Ultima APX-RS digital high-speed camera; a similar setup was proposed by Nishida et al. [53]. To obtain optimal images of the penetration process, it is necessary an appropriate lighting, which was provided

by an Arrisun 12 Plus lamphead with a 1200W Hydrargyrum Medium Arc Iodide (HMI) lamp.

In order to obtain pressure values inside the fluid, two pressure transducer (PCB 138A06) were located inside the tube. The position of the pressure gauges, near from the impact point (PTn) and far from the impact point (PTf), can be seen in Fig. 1 (b). In adittion six uniaxial strain gauges (350 Ohm, 2.120 Gage factor from Vishay Measurements Group Inc.) located at different points of the CFRP walls can also be seen in the Fig. 1 (b).

The projectile that impacts into the CFRP tubes consists on 12.5 mm diameter steel sphere; it is accelerated with a one stage light gas gun, capable of storing gas at a maximum pressure of 300 bar. The length of the barrel is 4.5 m and its calibre 25 mm. The specimen impacted was placed inside an armored steel chamber box $1 \times 1 \times 1$ m^3. The chamber had a small circular window in the front for the projectile to pass through, and two large lateral windows to illuminate the specimen and capture the video sequence of the impact. Two different impact velocities were performed: 600 and 900 m/s. Further information of the experimental tests and a complete detail of the results obtained can be found in [52].

3   Numerical implementation

The HRAM phenomenon is a highly non-linear transient dynamic problem, therefore the usage of an explicit finite element code is recommended to try to reproduce it. In this work, the commercial code Abaqus/Explicit v6.10 has been used to model the aforemention phenomenon and its effects on a CFRP tube. The nature of this problem makes really complex the employment of a lagrangian method in which the finite element mesh gets deformed jointly with the material. In situations in which deformation is extremely large, mesh gets distorted leading to numerical

problems (drop in explicit time step, worsening in results accuracy, error termination of simulations...). By the other hand, an Eulerian description allows the material to flow within a fixed mesh, avoiding mesh distortion problems. Therefore, in this work the fluid is modeled using an Eulerian description while a lagrangian description is used to model the surrounding structure and the projectile.

The drawback of this description is the presence of convection terms in the Eulerian equations [54]. The operator splitting proposed by Benson is a very efficient method for solving the Eulerian equations and it is implemented in the majority of the commercial finite element codes (also in ABAQUS). In this method, the step is divided into one Lagrangian step and one Eulerian. As a consequence of this, computational costs are higher than when only a lagrangian description is used. The coupling algorithm between both descriptions is performed by a penalty based contact algorithm [55]. Also, it must be taken into account that in order to let the fluid move through the Eulerian domain, the mesh must be shared between the fluid and other material or at least, void. As the Eulerian mesh is fixed in space, if only one material fills that mesh, no material movement will be seen in the simulations.

3.1 Carbon fibre woven epoxy laminates model

The behavior of the carbon/epoxy woven laminate has been modeled as an orthotropic elastic material until failure. This kind of approach has been widely used in impact problems on composite materials; some examples are the Hou et al. [56] model for tape laminates or the J. López-Puente et al. [13] model for woven laminates. To model how the material fails, different damage mechanism are defined: fiber failure, matrix failure and delamination. For each damage mechanism one or two scalars are defined by means of the actual stress tensor and the laminate strength properties; its value could vary from 0, which means no damage to 1 which

means fully damage. The mechanisms are:

- The fibre failure is described by means of d_{f1} and d_{f2}, one for each fibre direction:

$$
d_{f1} = \begin{cases} \dfrac{\sigma_{11}}{X_t} & if \ \sigma_{11} > 0 \\[3ex] \dfrac{|\sigma_{11}|}{X_c} & if \ \sigma_{11} < 0 \end{cases} \tag{1}
$$

$$
d_{f2} = \begin{cases} \dfrac{\sigma_{22}}{Y_t} & if \ \sigma_{22} > 0 \\[3ex] \dfrac{|\sigma_{22}|}{Y_c} & if \ \sigma_{22} < 0 \end{cases} \tag{2}
$$

where σ_{11} and σ_{22} are the stresses in the warp and fill direction respectively, X_t and X_c are the strengths of the composite laminate in tension and compression for the warp direction, and finally Y_t and Y_c are the strengths in tension and compression for the fill direction.

- For the matrix failure damage mechanism two parameters are defined, one in plane direction (d_{m12}), an the other one in the through-thickness direction (d_{m3}). The corresponding equations are:

$$
d_{m12} = \frac{\sigma_{12}}{S_{12}} \tag{3}
$$

$$
d_{m3} = \frac{1}{4}\left(\frac{\sigma_{33}}{Z_c}\right)^2 + \frac{Z_c \cdot \sigma_{33}}{4S_{13}S_{23}} + \left|\frac{\sigma_{33}}{Z_c}\right| + max\left[\left(\frac{\sigma_{13}}{S_{13}}\right)^2, \left(\frac{\sigma_{23}}{S_{23}}\right)^2\right] \tag{4}
$$

where σ_{ij} are components of the stress tensor, S_{12}, S_{13} and S_{23} are the shear strengths in the three different planes and finally Z_c is the strength in the through-thickness direction under compression. The Eq. (4) applies only when $\sigma_{33} < 0$. Eq. (4) is a modified version of the expression proposed by Hou et al. [56]for this

(a) Fiber Failure   (b) Matrix in plane failure   (c) Matrix Crushing and de-
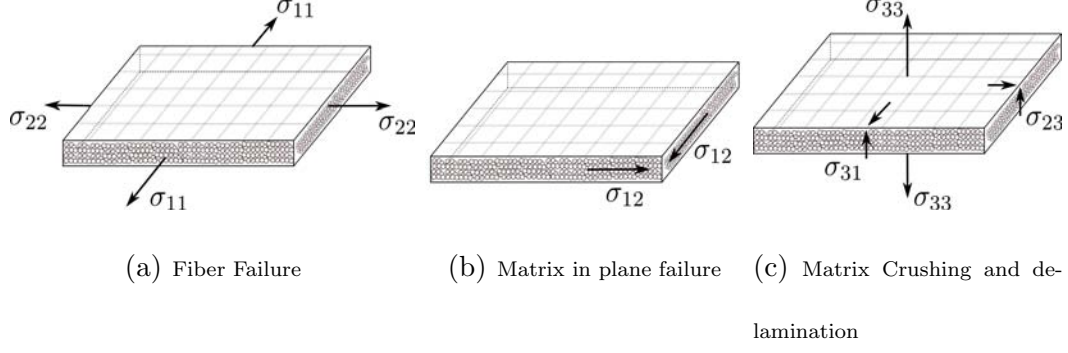
lamination

Fig. 2. Stress components that participates in each failure mode
mechanism for tape laminates.

- For the delamination failure mechanism one scalar is defined; the expression used
  is the same proposed by Hou et al.

$$d_{dela} = \left(\frac{\sigma_{33}}{Z_r}\right)^2 + \left(\frac{\sigma_{23}}{S_{23}}\right)^2 + \left(\frac{\sigma_{13}}{S_{13}}\right)^2 \qquad (5)$$

Where again σ_{ij} are components of the stresstensor, and Z_r is the strength in the
through-thickness direction under tension. This failure mechanism is computed
only when $\sigma_{33} > 0$.

Fig. 2 shows the stresses that participate in each failure mechanism. When the
value of one of the damage parameters described reaches the value of 1, the com-
ponents of the stress tensor σ_{ij} involved in the failure definition are set to zero.
To avoid numerical instabilities during the simulations due to sudden changes in
stiffness, a smooth transition is used. The Eq. (6) shows how the stress components
are modified as a function of the corresponding damage parameters defined. For the
numerical simulations accomplished in this work, the value $s = 45$ was adopted.

$$\sigma_{ij}^{cor} = \sigma_{ij}\left(1 - \frac{2 - e^{s(d_{ij} - 1/2)}}{2 - e^{s/2}}\right) \qquad (6)$$

The element erosion is controlled by the total strain; after each time increment the strain tensor is calculated, if one of the components reaches a critical value, then the element is removed. The properties of the carbon fibre woven laminates are presented in table 1.

	$E_1 = E_2$	E_3	ν_{12}
Elastic properties	68 GPa	10 GPa	0.22
	$\nu_{13} = \nu_{23}$	G_{12}	$G_{23} = G_{13}$
	0.49	5 GPa	4.5 GPa
	$X_t = Y_t = X_c = Y_c$	Z_c	Z_r
Strength properties	880 MPa	340 MPa	96 MPa
	S_{12}	S_{13}	S_{23}
	84 MPa	120 MPa	120 MPa
Critical strain	$\varepsilon_1 = \varepsilon_2$	ε_3	$\varepsilon_{12} = \varepsilon_{23} = \varepsilon_{13}$
	0.025	0.05	0.1

Table 1

Properties of woven carbon/epoxy laminate

3.2 Box and projectile lagrangian FE model

The model of the problem under consideration can be simplified attending to its symmetry, so that only a quarter of the problem has to be modeled obtaining a desirable reduction of the computational cost (Fig. 3 (a)). The solid parts involved

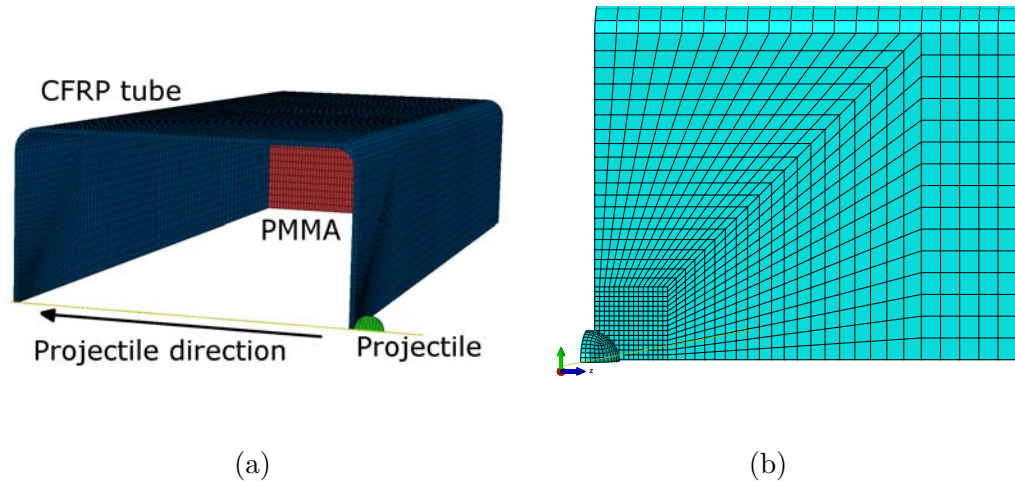in the problem, the projectile and the woven CFRP tube which is closed by the PMMA window, are modeled as follows.

(a)   (b)

Fig. 3. (a) Woven CFRP and projectile lagrangian mesh (b) Impacted zone mesh

- **Woven CFRP tube**. It is discretised by means of eight node linear solid elements with reduced integration and hourglass control, called C3D8R. Solid elements must be used in order to reproduce the perpendicular impact and penetration process into the woven CFRP tube. Mesh density is higher in the impacted zone ($1 \times 1 \, mm^2$) and it decreases with the distance from the impacted zone (until $7.3 \times 4.5 \, mm^2$), performing a mesh that accurately simulates the damage induced according to previous works [57]. A detailed of this refined zone can be seen in Fig. 3 (b). The CFRP tube walls present 5 elements through the thickness, so each element models two plies. The material model previously described in section 3.1 has been implemented through a user subroutine in order to reproduce the woven CFRP behavior.

- **Steel projectile and PMMA window**. The projectile is discretised by means of C3D8R, while the PMMA window is discretised by means of four node conventional shell elements with reduced integration (S4R). The element size of the projectile, although relatively bigger than those elements of the tube in which impacts, allows to solve in a properly way the contacts with the tank walls. Both,

steel and PMMA, are modeled as elastic materials since no plastic deformation nor damage is observed in none of them in the experimental tests. The material properties used in the model for PMMA and steel can be seen in the table 2.

Finally 46330 $C3D8R$ elements have been used for the woven CFRP tube, 400 $C3D8R$ elements for the steel projectile and 1968 $S4R$ elements for the PMMA window.

Steel	$\boldsymbol{\rho}$	$\boldsymbol{E}$	$\boldsymbol{\nu}$
	7850 Kg/m^3	210 GPa	0.3

PMMA	$\boldsymbol{\rho}$	$\boldsymbol{E}$	$\boldsymbol{\nu}$
	1180 Kg/m^3	3 GPa	0.35

Table 2

Steel and PMMA elastic properties

3.3 Eulerian fluid model

As it has been already mentioned, fluid is modeled using an eulerian description, avoiding numerical instabilities that would have appeared using a lagrangian approach.

The Eulerian domain used in the simulations can be seen in Fig. 4. The domain dimensions have been defined after several studies, so that the deformed CFRP tube walls never reach the boundary of the Eulerian domain. Therefore, the interaction between fluid and the surrounding structure is computed during the whole simulation being able of reproducing the effect of the HRAM phenomenon.

In order to allow the fluid inside the tube to flow around and interact with the structure, it is necessary to define a void mesh outside of the water mesh as it was
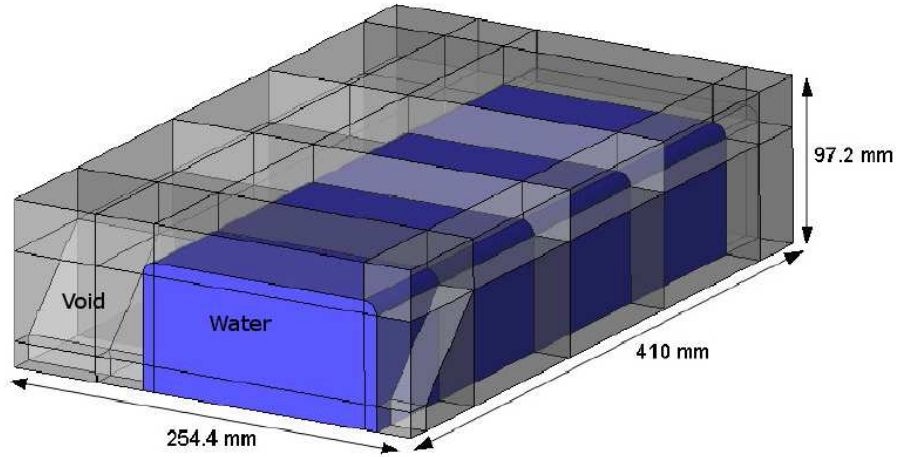
Fig. 4. Eulerian domain modeled

already mentioned, Fig. 4.

The whole Eulerian mesh is discretised by means of 8 node solids elements, multi-material, with reduced integration and hourglass control, called EC3D8R.

In order to assure an accurate contact between fluid and the surface of the woven CFRP tube walls, both parts were discretized with the same element size. This fact avoids possible leakage problems [58]. The element size of the fluid mesh was chosen according to previous studies regarding deceleration of an sphere inside a fluid. A simplified model without the CFRP tube was used to perform several impacts and compare the results of deceleration of the sphere for different element sizes with the theoretical case. The value of 2 mm have been chosen because it reproduces accurately the deceleration with a reasonable computational cost. Finally, 316734 Eulerian elements have been used in the model, Fig. 5.

As it was already mentioned, the interaction between the fluid and the structure is made through a coupling algorithm based on a penalty method. In Abaqus/Explicit this contact is used when the general contact option is active.

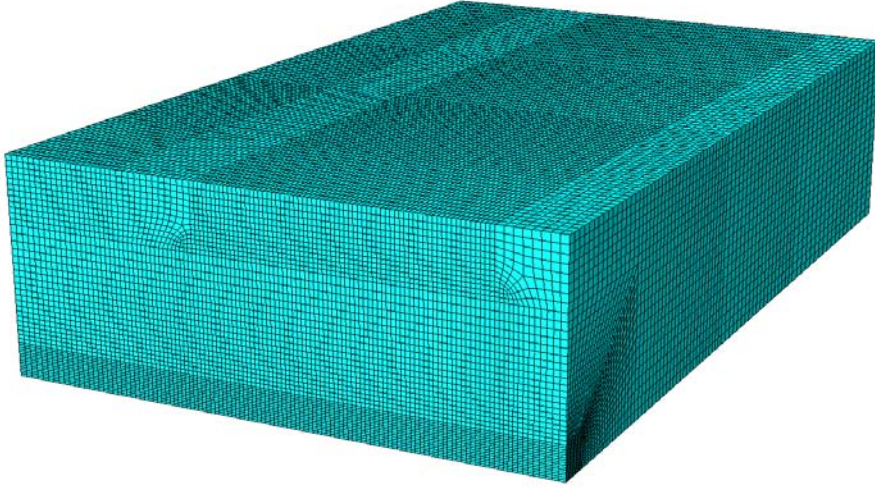When one material penetrates into another, the penalty methods acts introducing

Fig. 5. Eulerian mesh

the effect of a spring that moves the interfaces to a non-penetrating situation [55].

The fluid material behavior is defined by the following viscous constitutive equation [58]:

$$\sigma = 2\eta\dot{\varepsilon}' - P\,I \tag{7}$$

where η is the dynamic viscosity, $\dot{\varepsilon}'$ is the deviatoric strain rate, P is the pressure and I, the identity tensor. The pressure P is related with density ρ using a Mie-Grüneisen equation of state, where:

$$P = \frac{\rho_0\eta c^2}{(1 - s\eta)^2}(1 - \frac{\Gamma_0\eta}{2}) + \Gamma_0\rho_0 E_m \tag{8}$$

for compressed materials and

$$P = 0 \tag{9}$$

for expanded materials, avoiding negative pressure in the fluid. In Eq. (8), η is the nominal volumetric compressive strain $\eta = 1 - \rho_0/\rho$, ρ is the density and ρ_0 is the initial density; c is the speed of sound in water, and s is the slope of the

$u_s - u_p$ curve where u_s is the shock velocity and u_p is the particle velocity. Γ_0 is the Grüneisen gamma and E_m is the internal energy per unit of mass. Water properties are obtained from [59], see table 3.

Property	Unit	Value
ρ_0	$[kg/m^3]$	1000
c	$[m/s]$	1448
s	[-]	1.972
ν	$[Pa\ s]$	0.00089
Γ_0	[-]	0.11
E_m	$[J/Kg]$	920.9

Table 3

Water properties

4   Results

In order to validate the model, the experimental data of a completely filled tube impacted at 900 and 600 m/s, obtained by D. Varas et al. [52], will be compared with the numerical results. The capability of the CEL approach in Abaqus/Explicit to reproduce fluid-structure interaction problems, as well as the HRAM phenomenon, will be analyzed. In addition, the results regarding the effects in the CFRP structure will determine if the proposed material model is capable of reproducing the appropriate behavior of the tubes. Six validation variables have been identified: the qualitative reproduction of the HRAM stages, projectile position inside the tank, fluid pressure field, cavity evolution, CFRP strain values and final failure of tanks.

• **HRAM stages**. Fig. 6 shows how the numerical model qualitatively reproduces the four well known HRAM stages.
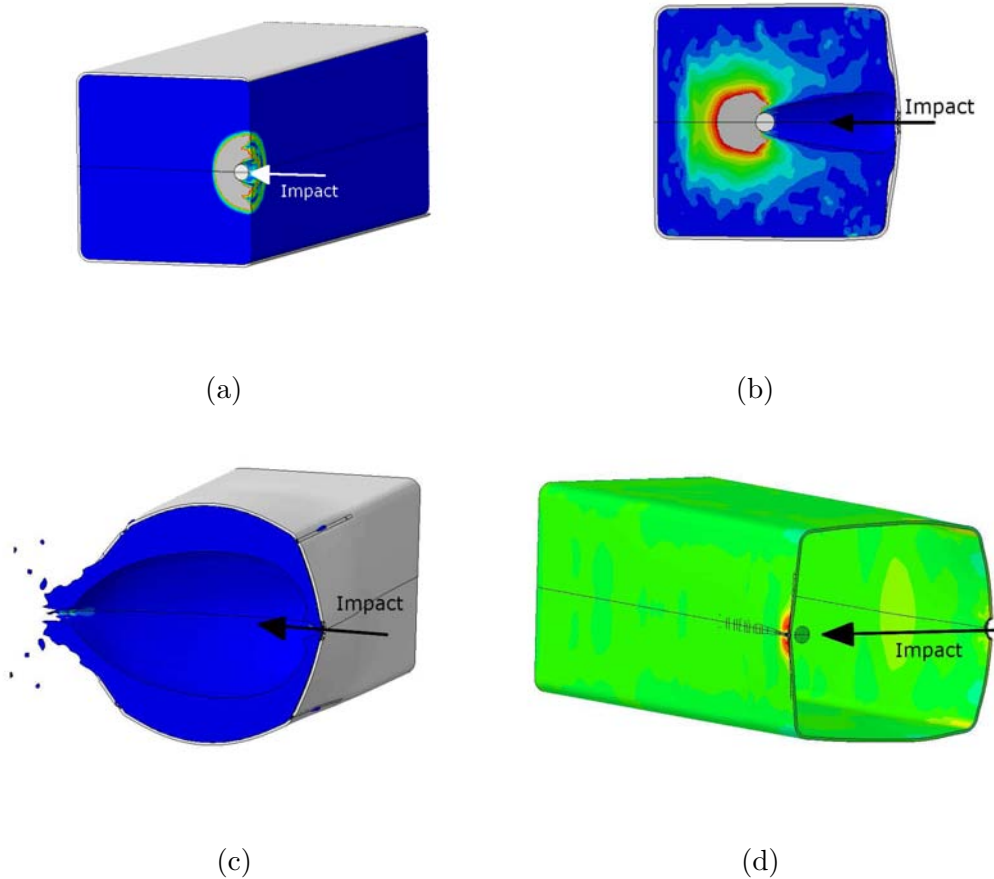

(a)

(b)

(c)

(d)

Fig. 6. Impact at $900 m/s$. (a) Pressure field at 20 μs after the impact. (b) Pressure field at 120 μs after the impact. (c) Pressure field at 1.2 ms after the impact. (d) Contour plot of stresses in fiber direction (σ_{11}) at 240 μs after the impact.

- Shock phase. The event that characterizes this stage is the hemispherical pressure wave produced due to the projectile impact and that is transmitted through the fluid to the whole structure. The mentioned pressure wave at 20 μs after the impact can be seen in Fig. 6 (a).
- Drag phase. The projectile, while travels through the tank, transmits part of its kinetic energy to the fluid; hence the fluid is displaced from the projectile path generating a radial pressure field and a cavity in the projectile wake, Fig.

6 (b).

- Cavity phase. This stage is represented by the growth of the cavity generated by the projectile. Fig. 6 (c) depicts the maximum size reached by the cavity. The cavity pushes the fluid against tube walls, inducing significant deformations in the structure. This stage is the main responsible for the most important damage effects on the structure. This is very well reproduced by the numerical model.

- Exit phase. The exit wall of the tank is pre-stressed before the projectile go through it. This is due to the initial shock stage and the subsequent loading by the fluid. Fig. 6 (d) shows how the model reproduce this behavior. The exit wall is already stressed before the projectile impact, which would explain why damage and strains are larger in the exit wall than in the entry one.

- **Projectile Position.** As it was already mentioned, the experimental projectile position can be obtained by means of the high-speed camera. This data have been compared with numerical and analytical projectile position, obtained integrating from Newton's second law [60].

$$m_p \frac{dV_p}{dt} = -\frac{1}{2}\rho_w A_0 C_d V_p^2 \tag{10}$$

where m_p and V_p are the projectile mass and velocity, ρ_w is the fluid density, A_0 is the projected frontal area of the projectile and C_d is a dimensionless drag coefficient. According to the range of velocities considered, a value of 0.4 for C_d was chosen.

The experimental and numerical time history of the projectile is depicted in Fig. 7. A good correlation between the curves it is observed, showing a maximum difference of about a 6%. The trend of the projectile velocity can be observed by means of the projectile position slope in Fig. 7. The velocity decreases inside the fluid, transforming part of its kinetic energy into pressure and kinetic energies in the fluid. As it was mentioned before, the projectile position correlation was

used to determine the mesh discretization in the projectile direction. It has to be noted that with a finer mesh, as other authors observed [58,61,62], better results can be obtained. Nevertheless instabilities in the contacts between the fluid and the structure as well as the computational cost growth, would made useless the improvement.
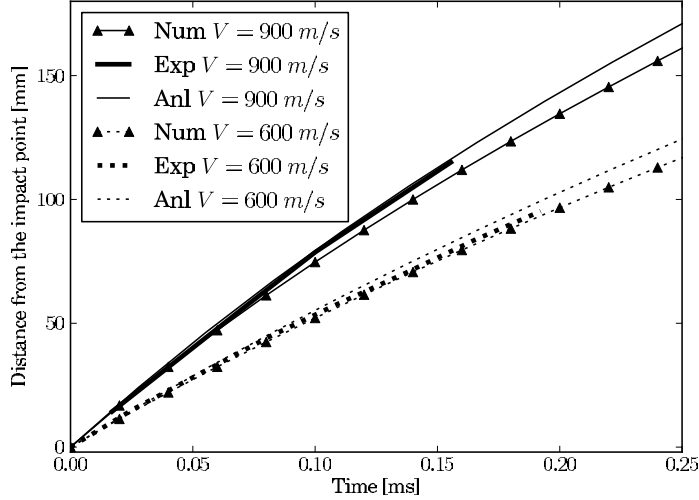

Fig. 7. Projectile position obtained analytically, numerically and experimentally at 900 and 600 m/s

- **Pressure field.** As was already mentioned, two pressure transducers were located inside the fluid at different positions; this allows knowing how the distance from the impact point affects the pressure generated in the fluid. One pressure transducer (PTn) was located at 30 mm from the wall and 75 mm away from the shot line, that is 81 mm from the impact point. The other transducer (PTf) was placed in the middle of the tube, 150 mm away from the projectile trajectory and 171 mm from the impact point, see Fig. 1 (b).

The pressure values obtained in the pressure transducers, both experimental and numerically, when a completely filled tube is impacted at different velocities are depicted in Fig. 8. A good correlation can be observed not only in peak values but in the trends regarding impact velocity and pressure transducer location
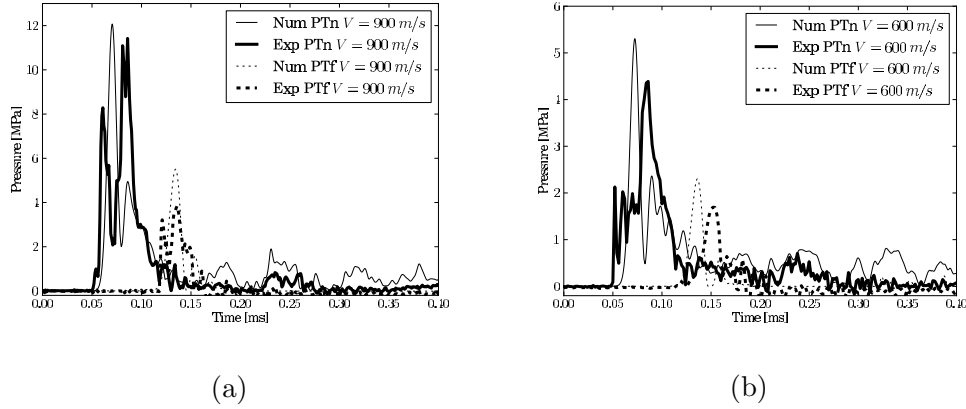
Fig. 8. Pressure time history near (PTn) and far (PTf) from impact point in a tube completely filled (a) impacted at 900 m/s (b) impacted at 600 m/s

influences. It can be observed how the intensity of the pressure wave increases with the impact velocity, being the pressure peak value at 900 m/s double than at 600 m/s; this result is related to the fact that the pressure is proportional to kinetic energy [24]. Pressure values in the far pressure transducer are smaller because the energy of an spherical pressure wave diminishes with the distance to its source. Nevertheless it has to be noted that better predictions are achieved in points near impact (PTn) than far from the impact (PTf); this is probably due to the fact that the mesh is finer near the impact point. As pressures are averaged over the elements, the usage of larger elements leads to lower values of pressure. Finally, the beginning of the pressure pulse is also well predicted by the numerical model.

- **Cavity evolution.** Since cavity is the main cause of the deformation and failure of the tanks, it is interesting to analyze how the cavity evolution is predicted by the numerical model. Numerical cavity evolution can be compared with the images of the penetration process recorded with the High-Speed Camera. In Fig. 9, experimental and numerical images at different impact velocities are shown. The images show the initiation and the subsequent growth of the cavity inside the fluid. Good correlation between experimental and numerical cavity evolution

is observed for both impact velocities, Fig. 9. Also, it can be seen that the cavity grows faster when the impact is at $900 m/s$, therefore the energy of the fluid is higher and the damage effects in the structure are more severe. According to that, deformation and final failure of the CFRP tank are influenced by the projectile velocity.

- **CFRP strain values.** As it has been said before, six uniaxial gauges were attached to the exterior surface of the CFRP tube. Two were located in the entry wall: G1 and G2 located at 50 mm and 150 mm from the impact point respectively. Other two strain gauges, G3 and G4, were located in the exit wall, in the same positions as G1 and G2. Finally two more gauges, G5 and G6, were located in the middle of the lower and upper wall, respectively (Fig. 1 (b)). A comparison between the numerical and experimental strain gauges results are shown in Figs. 10 - 12. It has to be mentioned that some of the experimental signals are not longer valid few time after the impact. This is due to the violent shake of the tube when it is impacted and/or the peeling of the outer plies, which may induced the debonding of the gauges. In addition, it is worth to say that the positive sign in strain data indicates that the wall is displaced outwards

Fig. 10 depicts the strain data at gauge G1 (closest gauge to the impact point) for a completely filled tube impacted at 900 and 600 m/s. Although the experimental data is no longer valid few time after impact, it can be observed that the numerical model reproduces the trend observed experimentally in the first instants of time. The strain data of gauge G2, placed in the entry wall far from the impact point, is shown in Fig. 11. It can be said that the numerical results are in accordance with the experimental data, both in maximum values and trends. Finally the strain time history in the middle of the upper wall and directly above the trajectory of the projectile (G5) is shown in Fig. 12. As in the other gauges, the numerical predictions agree with the trends observed experimentally. It has to be noted that the experimental curve obtained at 900 m/s, diminishes few
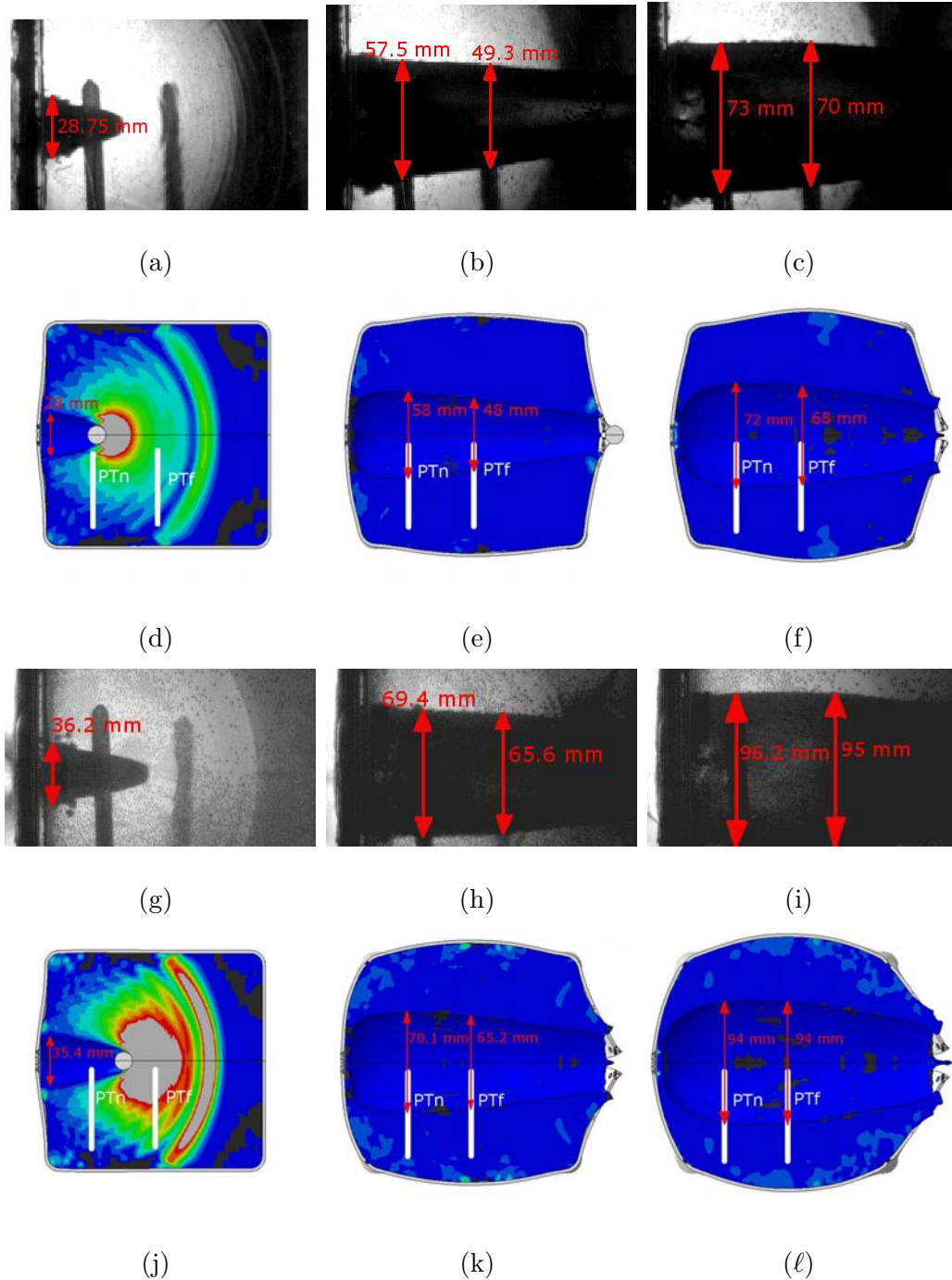
Fig. 9. Sequence of projectile penetration into the tube at 600 m/s and 900 m/s. Images taken from experiment at (a) 83 μs (b) 413 μs (c) 663 μs and from numerical simulation at (d) 80 μs, (e) 420 μs and (f) 660 μs. The images from the experimental impact at 900 m/s were taken at (g) 83 μs, (h) 413 μs and (i) 663 μs and the numerical impact at (j) 83 μs, (k) 413 μs and (l) 663 μs.

time after impact. This is probably due the effect of the crack that appears in the edge which provokes the relaxation of the wall as is pointed in [52]. Although the crack also appears in the numerical simulation, it does not affect the whole thickness of the tube wall, hence it is not deep enough to isolate the wall from the behavior of the rest of the tube. Finally it is worth to mention that the instant in which the maximum strain values appears in Figs. 11 and 12 matches with the time in which the maximum cavity size is reached (1.2 ms after the impact). This confirms the importance of the effect of the cavity in the behaviour of the structure, being more important than the pressure pulse.
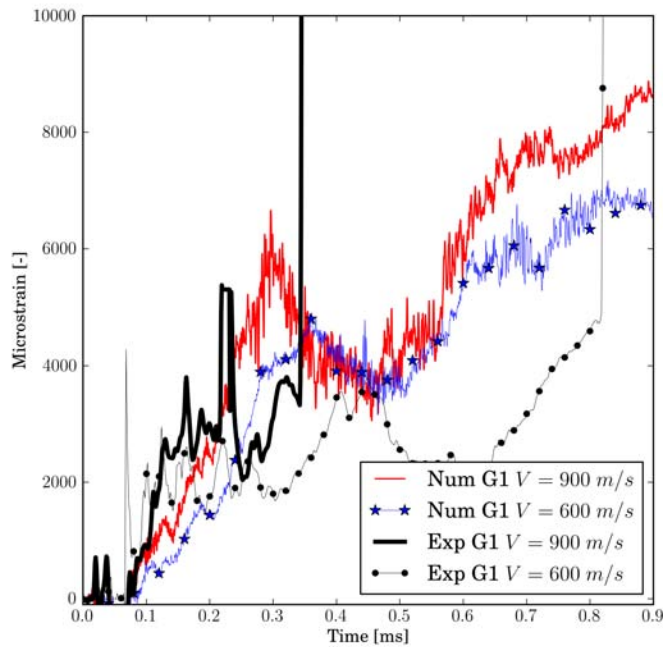

Fig. 10. Detail of the strain time history of G1 obtained numerically and experimentally at 900 and 600 m/s

- **Failure in tubes.** Due to the complexity of this process and the influence of CFRP manufacturing in the tube behavior, it is not easy to reproduce same experimental failure in numerical simulation. Nevertheless, similar trends can be seen in both experimental and numerical final failures. It can be seen in Fig. 13
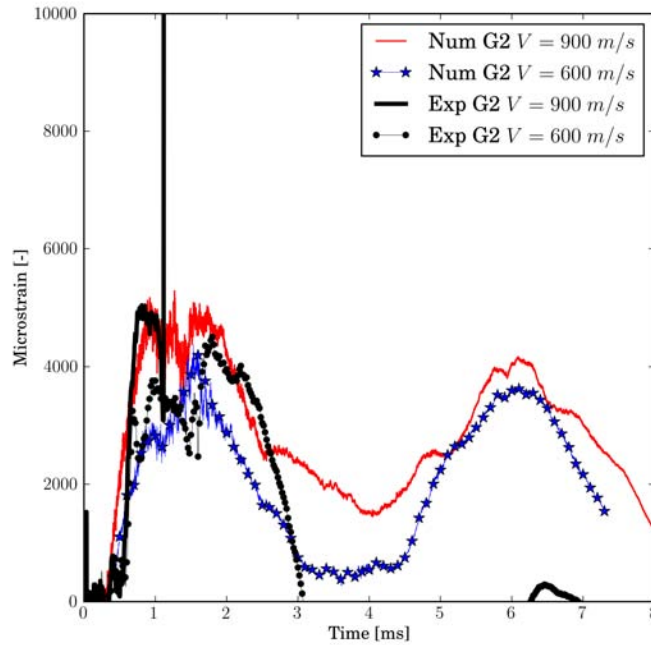
Fig. 11. Strain time history of G2 obtained numerically and experimentally at 900 and 600 m/s

that the most damaged area is the exit wall, where a cross-type failure appears. When the tube is impacted at a lower velocity, 600 m/s, the mentioned cross-type failure also appears in the exit wall with a smaller size, Fig. 14. This behavior can be seen both in the experimental and numerical impacts, although the numerical length is underestimated. Fig. 15 shows how the numerical model predicts the longitudinal crack that appears on the edge of the tube in experiments. In this case the model overestimates the length of such a crack.

5   Influence of velocity in HRAM effect

Once the numerical model has been validated with experimental results, the influence of velocity in HRAM phenomenon is analyzed using numerical simulations. Therefore, four numerical impacts have been simulated at different projectile ve-
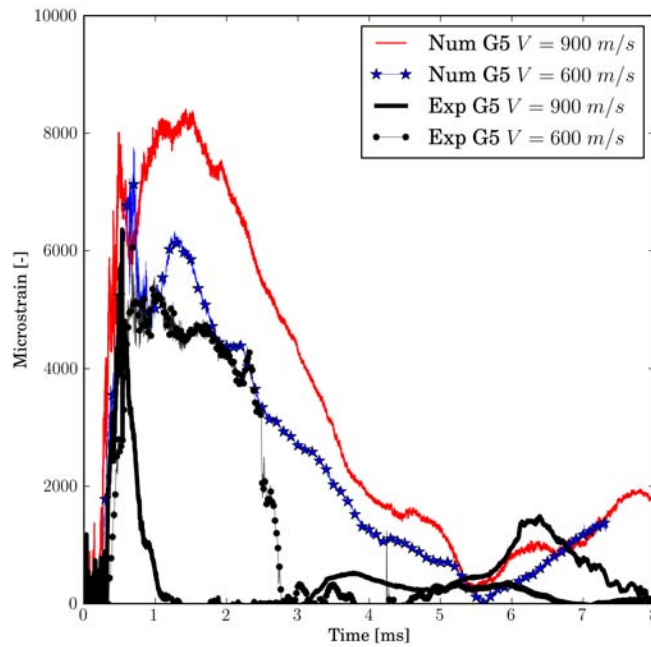
Fig. 12. Strain time history of G5 obtained numerically and experimentally at 900 and 600 m/s

(a)   (b)

Fig. 13. Final failure at the exit wall of the CFRP tube. $v = 900 \ m/s$

(a)   (b)

Fig. 14. Final failure at the exit wall of the CFRP tube. $v = 600 \ m/s$

locities (450, 600, 750 and 900 m/s). Maximum peak pressure wave, maximum size of cavity and failure in tubes are compared between the different impacts. Fig. 16 (a) shows the influence of the impact velocity on the maximum peak pressures, so

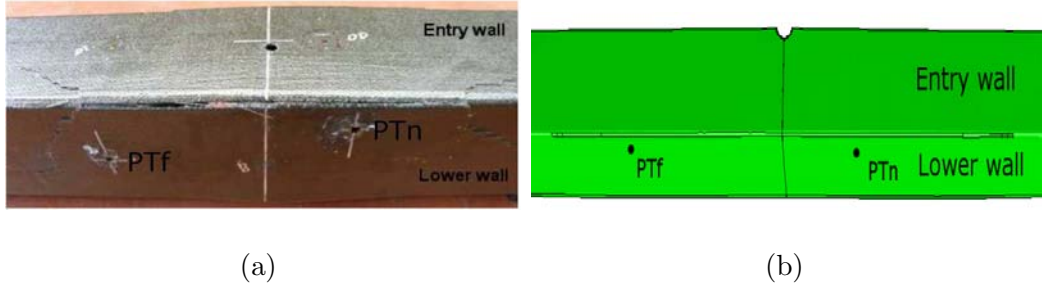<div align="center">(a)   (b)</div>

Fig. 15. Detail of the final failure of the CFRP tube at 900 m/s

that when the velocity is doubled, the pressure is approximately four times higher. Therefore, the pressure wave magnitude is proportional to the projectile kinetic energy as Lecysin et al. mentioned in [24]. In far pressure transducer the peak pressure is smaller, as it was already mentioned, because of the higher distance to the wave source. Fig. 16 (b) shows the relation between impact velocity and maximum cavity size. A linear relation between them can be observed until an impact velocity of 750 m/s is reached. Above this velocity, the slope is reduced due to the fact that the cavity is about the size of the tube. Therefore, when the impact velocity increases, the pressure and the cavity size increase causing a higher structural damage, as it can be seen in Figs. 17 and 18. Fig. 17 depicts the relation between the extent of vertical and horizontal cracks, caused by fiber failure in both in-plane axes, and the impact velocity. In Fig. 18, it can be seen the failures appeared in a quarter of the CFRP tube. No different failure mechanism can be observed in the four images, although a failure in the curved edge is observed at 900 m/s, Fig. 15.

6   Conclusions

The capability of the used numerical technique, CEL approach, in modeling the fluid structure interaction was analyzed, as well as the accuracy of the CFRP material model proposed, in reproducing the experimental failures appeared in a HRAM event. Numerical results were compared with the experimental ones obtained in a previous work done by Varas et al. [52]. In addition, various numerical impacts have
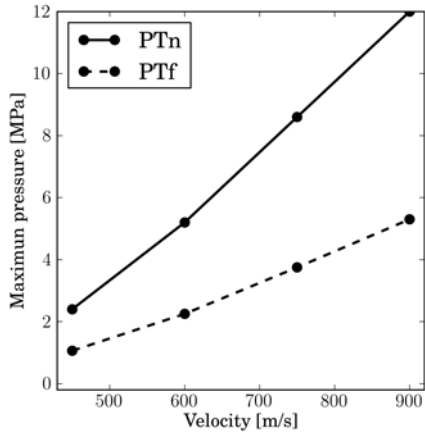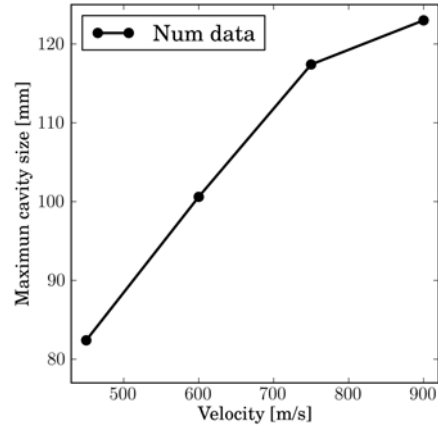
(a)   (b)

Fig. 16. a) Maximum pressure in impacts at 450 m/s, 600 m/s, 750 m/s and 900 m/s b) Maximum cavitation size in impacts at 450 m/s, 600 m/s, 750 m/s and 900 m/s. Obtained from numerical results.
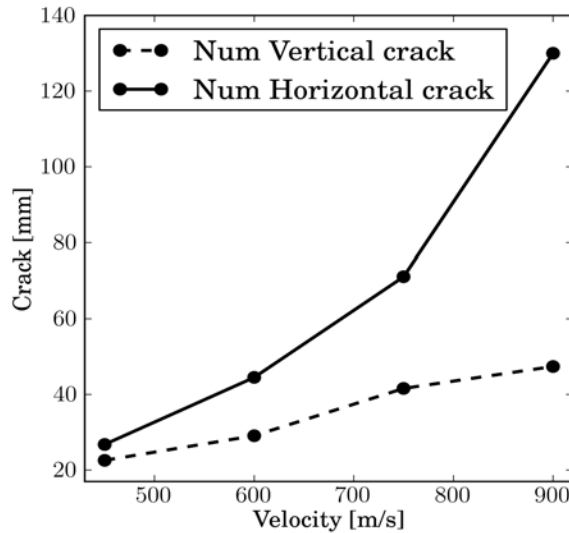

Fig. 17. Size of horizontal and vertical cracks appeared in a quarter of the exit wall in impacts at 450 m/s, 600 m/s, 750 m/s and 900 m/s. Obtained from numerical results.

been performed to analyze the influence of impact velocity in HRAM effects. Some conclusions have to be remarked:
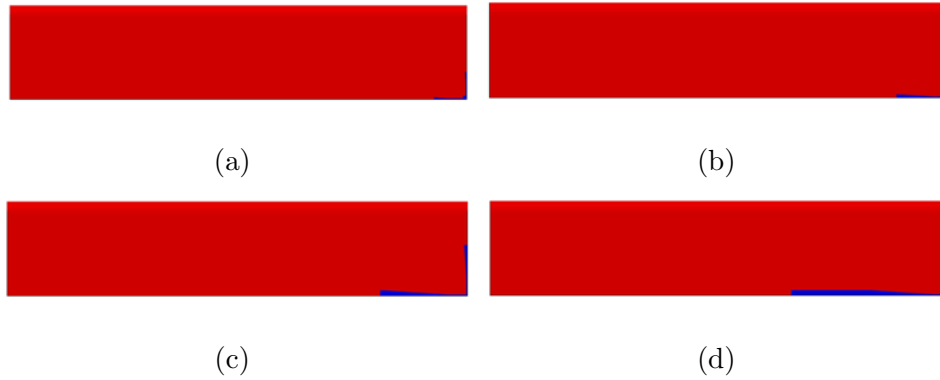
Fig. 18. Horizontal and vertical cracks, represented in blue, appeared in a quarter of the exit wall. a) 450 m/s b) 600 m/s c) 750 m/s d) 900 m/s. Obtained from numerical results.

- Coupled Eulerian Lagrangian approach implemented in ABAQUS/Explicit has been shown as a reliable tool to reproduce HRAM phenomenon. The model is able to reproduce HRAM stages: shock, drag, cavity and exit phases from qualitative and quantitative perspective. The projectile position is well captured, reproducing the energy exchange between the projectile and the fluid. The cavity evolution, main cause of the tank final failure, is accurately reproduced as compared with the images taken from the experimental tests.

- Water material model used reproduces accurately the peak values generated by the pressure wave in the fluid. Also it has been shown how the magnitude of the pressure wave diminishes with the distance from the impact point.

- The CFRP model, implemented by an user subroutine, reproduces the experimental failures in the most damaged area in the tube. It has been shown how the numerical strain values registered agrees with the trends observed experimentally. Also, strain measures registered, both numerical and experimental, shows that the maximum strain values occurs when the cavity has reached its maximum size, confirming the importance of the cavity effect in the behaviour of the structure and hence in the final tank failure.

- A higher velocity impact produce higher pressure peaks in shock phase and also

a larger cavity. Therefore, more damaging HRAM effects, as it is shown in experimental and numerical tests. The relation between magnitude of pressure pulse and impact velocity is quadratic, while maximum cavity size is linear.

Acknowledgements

References

[1] Tennyson RC. Composites in space - Challenges and opportunities, Proc ICCM 10, 1995, 1, p.35–56.

[2] Vasudev A, Meehlman J. A comparative study of the ballistic performance of glass reinforced plastic materials. SAMPLE Quart 1987; 18: 43-48.

[3] Cantwell WJ, Morton J. Influence of target geometry on the high velocity impact response of CFRP. Composite Structures 1988; 10: 247-265.

[4] Beaumont N, Penazzi L. The impact on a composite plate - a both theoretical and experimental approach of the inplane and transverse effects. Institute of Physics Conference Series 1989; 102: 411-418.

[5] Sun CT, Potti V. A simple model to predict residual velocities of thick composite laminates subjected to high velocity impact. International Journal of Impact Engineering 1996; 18: 339-353.

[6] Bland PW, Dear JP. Observations on the impact behaviour of carbon-fibre reinforced polymers for the qualitative validation of models. Composites Part A: applied science and manufacturing 2001; 32: 1217-1227.

[7] López-Puente J, Li S. Analysis of strain rate sensitivity of carbon/epoxy woven composites. International Journal of Impact Engineering, In press.

[8] López-Puente J, Zaera R, Navarro C. An analytical model for high velocity impacts on thin cfrps woven laminates. International Journal of Solids and Structures 2007; 44: 2837-2851.

[9] Wen HM. Penetration and Perforation of thick FRP laminates. Composites Science and Technology 2001; 61: 1163-1172.

[10] López-Puente J, Varas D, Loya JA, Zaera R. Analytical modelling of high velocity impacts of cylindrical projectiles on carbon/epoxy laminates. Composites Part A: applied science and manufacturing 2009; 40: 1223-1230.

[11] Bland PW, Dear JP. Observations on the impact behaviour of carbon-fibre reinforced polymers for the qualitative validation of models. Composites Part A: applied science and manufacturing 2001; 32: 1217-1227.

[12] López-Puente J, Zaera R, Navarro C. The effect of low temperatures on the intermediate and high velocity impact response of CFRP. Composites: Part B 2002 33: 559-566.

[13] López-Puente J, Zaera R, Navarro C. Experimental and numerical analysis of normal and oblique ballistic impacts on thin carbon/epoxy woven laminates. Composites Part A: applied science and manufacturing 2008; 39: 374-387.

[14] Fern´andez-Fdz D, L´opez-Puente J, Zaera R. Prediction of the behaviour of CFRPs against high-velocity impact of solids employing an artificial neural network methodology. Composites Part A: applied science and manufacturing 2008; 39:, 989-996.

[15] Hemmi K, Nishikawa M, Takeda N. Prediction of the foreign-object impact force on the composite fan blade. Design, Manufacturing and Applications of Composites: Proceedings of the Seventh Joint Canada-Japan Workshop on Composites 2008; 1: 101-108.

[16] Raimondo L, Iannucci L, Robinson P, Pinho ST. A Numerical Material Model for Predicting the High Velocity Impact Behaviour of Polymer Composites. Mechanical Response of Composites 2008; 10: 161-177.

[17] Nishikawa M, Okabe T, Takeda N. Numerical simulation of interlaminar damage propagation in CFRP cross-ply laminates under transverse loading. International Journal of Solids and Structures 2007; 44: 3101-3113.

[18] Airoldi A, Cacchione B. Modelling of impact forces and pressures in Lagrangian bird strike analyses. International Journal of Impact Engineering 2006; 32: 1651-1677.

[19] Anghileri M, Castelleti LML, Invernizzi F, Mascheroni M. A survey of numerical models for hail impact analysis. International Journal of Impact Engineering 2005; 31: 929-944.

[20] Mines RAW, McKown S, Birch RS. Impact of aircraft rubber tyre fragments on aluminium alloy plates: I-experimental. International Journal of Impact Engineering 2007; 34: 627-646.

[21] Santini P, Palmieri D, Marchetti M. Numerical simulation of fluid-structure interaction in aircraft fuel tanks subjected to hydrodynamic ram penetration. Proc 21st ICAS Congress, Melbourne, Australia, 1998.

[22] Lecysyn N, Dandrieux A, Heymes F, Slangen P, Munier L, Lapebie E, Le Gallic C, Dusserre G. Preliminary study of ballistic impact on an industrial tank: Projectile velocity decay. Journal of Loss Prevention in the Process Industries 2008; 21: 627-634.

[23] Lecysyn N, Dandrieux A, Heymes F, Aprin L, Slangen P, Munier L, Le Gallic C, Dusserre G. Ballistic impact on an industrial tank: Study and modeling of consequences. Journal of Hazardous Materials 2010; 172: 587-594.

[24] Lecysyn N, Bony-Dandrieux A, Aprin L, Heymes F, Slangen P, Dusserre G, Munier L, Le Gallic C. Experimental study of hydraulic ram effects on a liquid storage tank: Analysis of overpressure and cavitation induced by a high-speed projectile. Journal of Hazardous Materials 2010; 178: 635-643.

[25] Ball RE. A Computer Program for the Geometrically Nonlinear Static and Dynamic Analysis of Arbitrarily Loaded Shells of Revolution. Theory and User´s Manual. NASA CR-1987.

[26] Ball RE. Aircraft Fuel Tank Vulnerability to Hydraulic Ram: Modification of the Northrup Finite Element Computer Code BR-1 to include Fluid-Structure Interaction. Theory and User´s Manual for BR-1HR, NPS-57B p74071, July 1974.

[27] Lundstrom EA. Fluid/Structure Interaction in Hydraulic Ram, in: Proceedings of the Hydrodynamic Ram Seminar 1977; 1: 223-230.

[28] Herlin WM, Avery JG, Hydraulic Ram Structural Response Computer Program (HRSR), Boeing Co., Prepared under Contract N60530-80-C-0242 for Naval Weapons Center, China Lake, California.

[29] Freitas CJ, Anderson Jr CE, Walker JD, Littlefield DL. Hydrodynamic Ram: A Benchmark Suite, Structures Under Extreme Loading Conditions, PVP-Vol. 325., New York, ASME 1996, p. 63-74.

[30] Seddon CM, Moodie K, Thyer AM, Moatamedi M. Preliminary analysis of fuel tank impact. International Journal of Crash 2004; 9: 237-244.

[31] Anghileri M, Castelleti LML, Tirelli M. Fluid-structure interaction of water filled tanks during the impact with the ground. International Journal of Impact Engineering 2005; 31: 235-254.

[32] Jarzab WW, Chwalinski R, Pfrang WE, Tokar G. Fluid-structure interaction effects in tank structures due to sloshing and hydrodynamic ram Coupled Lagrangian-Eulerian simulations., Proc. International Conference: Spacecraft Structures and Mechanical Testing., Noordwijk, The Netherlands, 1988

[33] Souli M, Olovsson L, Do I. ALE and Fluid-Structure Interaction Capabilities in LS-DYNA, 7th International LS-DYNA Users Conference, Dearborn, Michigan, May 19-21, 2002.

[34] Fasanella EL, Boinott RL, Kellas S. Test and Analysis Correlation of High Speed Impacts of Ice Cylinders, 9th International LS-DYNA Users Conference, Dearborn, Michigan, June 4-6, 2006.

[35] Børvik T, Hanssen AG, Langseth M, Olovsson L. Response of structures to planar blast loads: A finite element engineering approach. Computers and Structures 2009; 87: 507-520.

[36] Lu Y, Wang Z. Characterization of structural effects from above-ground explosion using coupled numerical simulation. Computers and Structures 2006; 84: 1729-1742.

[37] Kim J, Shin H. Application of the ALE technique for underwater explosion analysis of a submarine liquefied oxygen tank. Ocean Engineering 2008; 35: 812-822.

[38] Marklund PO, Nilsson L. Simulation of airbag deployment using a coupled fluid-structure approach, in proc: 7th International LS-DYNA Users Conference,

Dearborn, Michigan, May 19-21, 2002.

[39] Koishi M, Okano T, Olovsson L, Saito H, Makino M. Hydroplaning simulation using fluid-structure interaction in LS-DYNA, in: 9th International LS-DYNA Users Conference, Dearborn, Michigan, June 4-6, 2006.

[40] Hanssen AG, Girard Y, Olovsson L, Berstad T, Langseth M. A numerical model for bird strike of aluminium foam-based sandwich panels. International Journal of Impact Engineering 2006; 32: 1127-1144.

[41] Jenq ST, Hsiao FB, Lin IC, Zimcik DG, Nejad Ensan M. Simulation of a rigid plate hit by a cylindrical hemi-spherical tip-ended soft impactor. Computational Materials Science 2007; 39: 518-526.

[42] Zhang A, Suzuki K. A comparative study of numerical simulations for fluid-structure interaction of liquid-filled tank during ship collision. Ocean Engineering 2007; 34: 645-652.

[43] Bathe KJ, Zhang H, Ji S. Finite element analysis of fluid flows fully coupled with structural interactions. Computers and Structures 1999; 72: 1-16.

[44] Unger R, Haupt MC, Horst P. Application of Lagrange multipliers for coupled problems in fluid and structural interactions. Computers and Structures 2007; 85: 796-809.

[45] Vierendels J, Lanoye L, Degroote J, Verdonck P. Implicit coupling of partitioned fluid-structure interaction problems with reduced order models. Computers and Structures 2007; 85: 970-976.

[46] Kayser-Herold O, Matthies HG. A unified least-squares formulation for fluid-structure interaction problems. Computers and Structures 2007; 85: 998-1011.

[47] Tai CH, Liew KM, Zhao Y. Numerical simulation of 3D fluid-structure interaction flow using an immersed object method with overlapping grids. Computers and Structures 2007; 85: 749-762.

[48] Lee K, Noguchi H, Koshizuka S. Fluid-shell structure interaction analysis by coupled particle and finite element method. Computers and Structures 2007; 85: 688-697.

[49] Petitpas F, Massoni J, Saurel R, Lapebie E, Munier L. Diffuse interface model for high speed cavitating underwater systems. International Journal of Multiphase Flow 2009; 35: 747-759.

[50] Varas D, Zaera R, López-Puente J. Numerical modelling of partially filled aircraft fuel tanks submitted to Hydrodynamic Ram. Aerospace Science and Technology 2012; 16: 19-28.

[51] Varas D, López-Puente J., Zaera R. Numerical analysis of the Hydrodynamic Ram phenomenon in aircraft fuel tanks. AIAA Journal, In Press.

[52] Varas D, Zaera R, López-Puente J. Experimental study of fluid-filled tubes subjected to high-velocity impact. Composite Structures 2011; 93: 2598-2609.

[53] Nishida M, Tanaka K. Experimental study oof perforation and cracking of water-filled aluminum tubes impacted by steel spheres. International Journal of Impact Engineering 2006; 32: 2000-2016.

[54] Benson DJ. Computational methods in Lagrangian and eulerian Hydrocodes. Computer methods in applied mechanics and engineering 1992; 99: 235-394.

[55] Benson DJ, Okazawa S. Contact in a multi-material Eulerian finite element formulation. Computer methods in applied mechanics and engineering 2004; 193: 4277-4298.

[56] Hou P, Petrinic N, Ruiz C, Hallett SR. Prediction of impact damage in composite plates. Composites Science and Technology 2000; 60: 273-281.

[57] López-Puente J, Zaera R, Navarro C. High energy impact on woven laminate. Journal of Physics IV 2003; 110: 639-644.

[58] Varas D, Zaera R, L´opez-Puente J. Numerical modelling of the Hydrodynamic Ram phenomenon. International Journal of Impact Engineering 2009; 36: 363-374.

[59] Boyd R, Royles R, El-Deeb KMM. Simulation and validation of UNDEX phenomena relating to axisymmetric structures. Sixth international LS-DYNA users conference similation 2000: Dearborn, Michigan April 9-11.

[60] Varas D, Zaera R, López-Puente J. Experimental analysis of fluid-filled aluminium tubes subjected to high-velocity impact. International Journal of Impact Engineering 2008; 36: 81-91.

[61] Kim JH, Shin HC. Application of the ALE technique for underwater explosion analysis of a submarine liquefied oxygen tank. Ocean Engineering 2008; 35: 812-822.

[62] Poehlmann-Martins F, Gabrys J, Souli M. Hydrodynamic ram analysis of nonexploding projectile impacting water. ASME Pressure Vessels and Piping Division Conference 2005; Denver, Colorado.